ACS NANO

www.acsnano.org

ARTICLE

Super- and Subradiant Lattice Resonances in Bipartite Nanoparticle Arrays

Alvaro Cuartero-González, Stephen Sanders, Lauren Zundel, Antonio I. Fernández-Domínguez, and Alejandro Manjavacas*

Cite This: *ACS Nano* 2020, 14, 11876–11887

Read Online

ACCESS | Metrics & More | Article Recommendations | Supporting Information

ABSTRACT: Lattice resonances, the collective modes supported by periodic arrays of metallic nanoparticles, give rise to very strong and spectrally narrow optical responses. Thanks to these properties, which emerge from the coherent multiple scattering enabled by the periodic ordering of the array, lattice resonances are used in a variety of applications such as nanoscale lasing and biosensing. Here, we investigate the lattice resonances supported by bipartite nanoparticle arrays. We find that, depending on the relative position of the two particles within the unit cell, these arrays can support lattice resonances with a super- or subradiant character. While the former result in large values of reflectance with broad lineshapes due to the increased radiative losses, the latter give rise to very small linewidths and maximum absorbance, consistent with a reduction of the radiative losses. Furthermore, by analyzing the response of arrays with finite dimensions, we demonstrate that the subradiant lattice resonances of bipartite arrays require a much smaller number of elements to reach a given quality factor than the lattice resonances of arrays with single-particle unit cells. The results of this work, in addition to advancing our knowledge of the optical response of periodic arrays of nanostructures, provide an efficient approach to obtain narrow lattice resonances that are robust to fabrication imperfections.

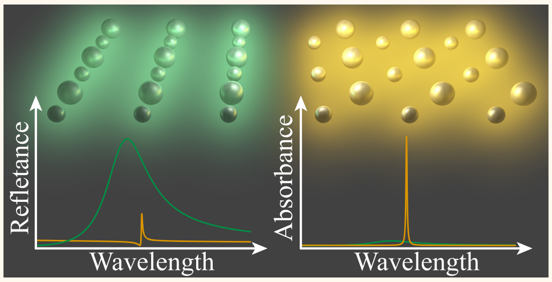

KEYWORDS: *lattice resonances, periodic arrays, nanoparticle arrays, ultranarrow, bipartite unit cell, plasmons, plasmonic crystals*

Metallic nanostructures have become exceptional tools to manipulate light at the nanoscale due to their ability to support surface plasmons.[1] These excitations, which emerge from the collective motion of the conduction electrons of the nanostructure, interact strongly with light and confine it into subwavelength volumes. As a consequence, surface plasmons produce large field enhancements[2] that have been exploited in a variety of applications including solar energy harvesting,[3] photocatalysis,[4] and photothermal cancer therapies.[5] However, due to their the large radiative cross sections, together with the inherent nonradiative losses of metals, the surface plasmons of individual nanostructures usually display relatively broad lineshapes, with quality factors (*i.e.*, the ratio of the central wavelength of the resonance to its width[6]) in the range $Q \lesssim 10-20$.[7,8] Although surface plasmons with a large bandwidth are useful for certain applications, there are many others, such as biosensing[9] and nanoscale light emission,[10] that would benefit from surface plasmons with large Q factors.

One way to obtain narrower plasmon resonances is to exploit the interaction between the plasmon excitations supported by individual metallic nanostructures. When arranged in appropriate geometries, the collective plasmonic modes resulting from this interaction can display a super- or subradiant character.[11−16] Superradiant (or bright) modes are characterized by a large net dipole moment arising from the sum of the dipole moments of the plasmons supported by the individual constituents. On the other hand, for subradiant (or dark) modes, the dipole moments of the individual constituents cancel one another, resulting in a smaller net dipole. As a consequence, the radiative losses of subradiant modes are significantly decreased with respect to those of the plasmons of the individual nanostructures, thus leading to narrower lineshapes and larger Q factors.[17−20] Oftentimes, super- and subradiant modes spectrally overlap, giving rise to asymmetric spectral features known as Fano resonances.[21−24]

An alternative approach to obtain strong and narrow resonances using metallic nanoparticles involves their arrange-

Received: June 8, 2020
Accepted: August 14, 2020
Published: August 14, 2020

https://dx.doi.org/10.1021/acsnano.0c04795

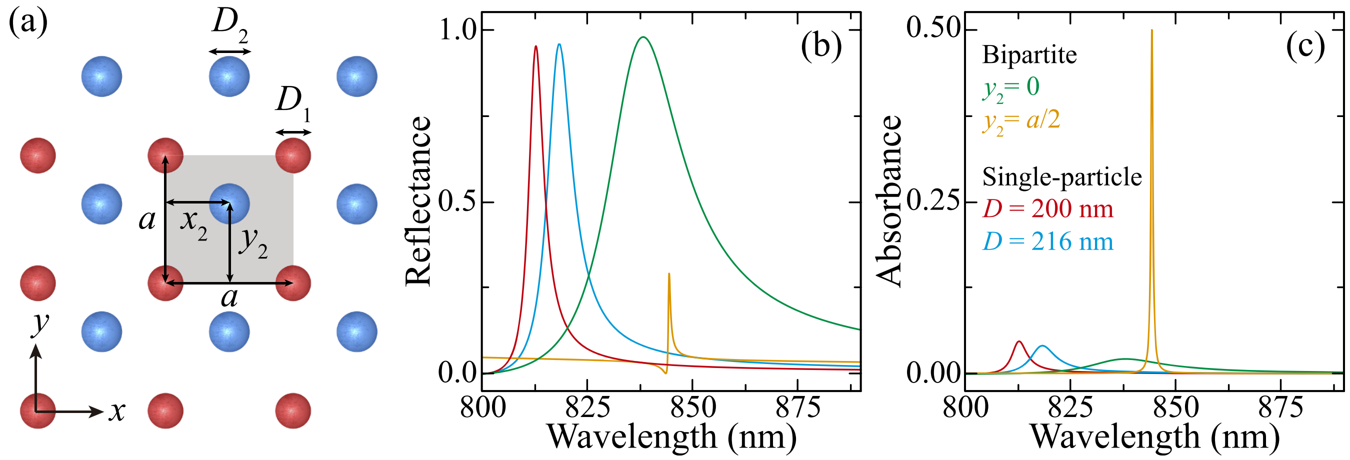

Figure 1. Sub- and superradiant lattice resonances in bipartite nanoparticle arrays. (a) Sketch of the system under study, built from the periodic repetition of a unit cell containing two silver nanospheres (shaded area) over a square lattice with periodicity a. Particle 1 (red), which has diameter D_1, is placed at the origin of the unit cell, while particle 2 (blue), with diameter D_2, is located at a position (x_2, y_2). (b, c) Reflectance (b) and absorbance (c) spectra for a bipartite array with a = 800 nm, D_1 = 200 nm, and D_2 = 216 nm. Green and yellow curves correspond to $y_2 = 0$ and $y_2 = a/2$, respectively, while $x_2 = a/2$ in both cases. For comparison, we plot the reflectance and absorbance of a single-particle array with the same periodicity a, made of particles with diameter D = 200 nm (red curve) or D = 216 nm (blue curve). Unless otherwise noted, in all of the cases discussed in this work, we assume illumination at normal incidence with polarization along the x-axis.

ment in a periodic array. These systems support collective modes known as lattice resonances, which arise from the coherent multiple scattering enabled by their periodic order and display large Q factors.[25−39] Indeed, a recent work has measured a quality factor of ~2400 in a single-particle array.[40] Thanks to these extraordinary properties, periodic arrays of metallic nanoparticles are being used for applications ranging from the design of different optical elements such as light-emitting devices,[10,41−50] lenses,[51] and color filters[52−54] to the implementation of ultrasensitive sensors[55−57] and platforms for exploring new physical phenomena.[58−62]

In this paper, we explore the possibility of combining these two approaches by investigating the lattice resonances supported by bipartite arrays.[29,63−65] We show that, depending on the relative position of the two particles within the unit cell, the lattice resonances supported by the array display a super- or subradiant character. Not surprisingly, each of these two behaviors leads to a very distinct optical response. Specifically, superradiant lattice resonances produce large values of reflectance with broad lineshapes, as expected from their increased radiative losses. On the other hand, the significant reduction of the radiative losses associated with the subradiant lattice resonances gives rise to very small linewidths with maximum absorbance. Furthermore, by analyzing the evolution of the optical response of finite arrays with an increasingly large number of unit cells, we demonstrate that the subradiant lattice resonances of bipartite arrays require a much smaller number of elements to reach a given quality factor than the lattice resonances supported by arrays with single-particle unit cells. This makes them less sensitive to finite-size effects and, hence, more robust to fabrication imperfections. Therefore, in addition to providing a comprehensive analysis of the response of bipartite arrays of nanoparticles, our results show an alternative path to achieve robust lattice resonances with large quality factors, thus complementing previous works based on the use of lattice resonances with an out-of-plane character[66−68] or associated with higher-order plasmon modes of the metallic nanostructures.[69−77]

RESULTS AND DISCUSSION

The system under study, which is depicted in Figure 1a, consists of a periodic array built from the repetition of a unit cell containing two silver nanoparticles (shaded area) over a square lattice of period a. Particle 1 (red), with diameter D_1, is placed at the origin of the unit cell $\mathbf{r}_1 = (0, 0)$, while particle 2 (blue), which has diameter D_2, is located at a position $\mathbf{r}_2 = (x_2, y_2)$ with x_2 always being $a/2$, as shown in the diagram. We are interested in the optical response of the array due to the lowest-order lattice resonance, which, under normal incidence illumination, occurs in the spectrum at wavelengths satisfying $\lambda > a$. Therefore, assuming that the size of the nanoparticles is much smaller than the lattice period a and, consequently, the relevant wavelengths, we can describe the response of the system in the dipolar limit using the coupled dipole model (CDM).[25,27,78] Within this approximation, we model each of the particles in the array as a point electric dipole with polarizability α, which we obtain from the dipolar Mie scattering coefficient[79] using a tabulated dielectric function.[80] We assume that the array is illuminated with an external field of amplitude E_0, which propagates along the z-axis (*i.e.*, perpendicularly to the array) and is polarized along the x-axis. Under such conditions, and due to the square symmetry of the array, the dipole induced in the nanoparticles is also polarized along the x-axis. Therefore, following our previous work on arrays with multiparticle unit cells[81] (see also refs. 82, 83, and 84), we can write the x-component of dipole induced in a given nanoparticle as

$$p_{i,\mu} = \alpha_i E_0 + \alpha_i \sum_{\nu}{}' \sum_{j=1}^{2} G_{ij,\mu\nu} p_{j,\nu} \tag{1}$$

where we use Greek indices to denote the unit cell to which the particle belongs and Latin ones to label each of the two particles within the unit cell. Furthermore, the prime in the first summation indicates that the terms $\nu = \mu$ are excluded from it when $i = j$, since a dipole does not interact with itself, and $G_{ij,\mu\nu}$ is the xx-component of the dipole−dipole interaction tensor, defined as

$$G_{ij,\mu\nu} = [k^2 + \partial_x\partial_x]\frac{e^{ik|\mathbf{T}_\mu + \mathbf{r}_i - \mathbf{T}_\nu - \mathbf{r}_j|}}{|\mathbf{T}_\mu + \mathbf{r}_i - \mathbf{T}_\nu - \mathbf{r}_j|}$$

with $\mathbf{T}_\mu - \mathbf{T}_\nu$ being the vector connecting the μ and ν unit cells and $k = 2\pi/\lambda$ the wavenumber. Thanks to the periodicity of the array, eq 1 admits a solution in the form of Bloch waves with amplitude (see the Methods)

$$\begin{bmatrix} p_1 \\ p_2 \end{bmatrix} = \frac{E_0}{F}\begin{bmatrix} \alpha_2^{-1} - \mathcal{G}_{11} + \mathcal{G}_{12} \\ \alpha_1^{-1} - \mathcal{G}_{11} + \mathcal{G}_{12} \end{bmatrix} \tag{2}$$

Here, $F = (\alpha_1^{-1} - \mathcal{G}_{11})(\alpha_2^{-1} - \mathcal{G}_{11}) - \mathcal{G}_{12}^2$ and $\mathcal{G}_{ij} = \sum_\nu' G_{ij,\nu 0}$ is the Fourier transform of the dipole−dipole interaction tensor, usually known as the lattice sum.[27,81] This quantity, which only depends on the geometry of the array, contains the information of the interaction between its elements. In particular, it diverges at the Rayleigh anomalies, which, for normal incidence, appear at wavelengths $\lambda_\mathbf{q} = 2\pi/|\mathbf{q}|$, with $\mathbf{q}$ representing the reciprocal lattice vectors of the array. Therefore, the lattice sum determines the existence of the lattice resonances, which emerge on the red side of the Rayleigh anomalies, corresponding to the poles of the total dipole induced in the unit cell $p = p_1 + p_2$.[38,78,81] As expected, the expression of p given in eq 2 reduces to the result for an array with a single-particle unit cell,[38,78,81]

$$p = \frac{E_0}{\alpha^{-1} - \mathcal{G}_{11}} \tag{3}$$

when one of the two particles is removed.

The optical response of the array can be characterized by analyzing its reflectance, $\mathcal{R}$, and absorbance, $\mathcal{A}$. As shown in the Methods, these two quantities can be written in terms of p, for $\lambda > a$, as

$$\mathcal{R} = |p|^2/(2\Pi_0)^2, \quad \mathcal{A} = \mathrm{Im}\{p\}/\Pi_0 - 2|p|^2/(2\Pi_0)^2 \tag{4}$$

where $\Pi_0 = a^2\lambda E_0/(8\pi^2)$. Using these expressions, we calculate the reflectance and the absorbance for two different bipartite arrays. Both of them have the same period $a = 800$ nm and particle sizes $D_1 = 200$ nm and $D_2 = 216$ nm. However, for one of them, particle 2 is located at $y_2 = 0$, while, for the other, it is placed at $y_2 = a/2$. The corresponding results are shown in Figure 1b,c, with green curves for $y_2 = 0$ and yellow ones for $y_2 = a/2$. They are in perfect agreement with rigorous solutions of Maxwell's equations obtained using a finite element method (FEM), as shown in Figure S1 of the Supporting Information. Clearly, both bipartite arrays support a lattice resonance; however, their optical properties are very different. Specifically, the lattice resonance of the array with $y_2 = 0$ gives rise to a very large reflectance, $\mathcal{R} \sim 0.98$, and an almost negligible absorbance, $\mathcal{A} \sim 0.02$, both with a significantly broad lineshape. On the contrary, the bipartite array with $y_2 = a/2$ supports a very narrow lattice resonance, resulting in a moderate reflectance, $\mathcal{R} \sim 0.29$, and an absorbance that almost saturates the theoretical limit for two-dimensional systems, $\mathcal{A} = 0.5$.[85] These characteristics coincide with the behavior expected for a super- and subradiant lattice resonance resulting from the hybridization of the lattice resonances supported by the two single-particle arrays into which these bipartite arrays can be divided. Indeed, analyzing the reflectance and absorbance of a single-particle array with the same periodicity, made of particles with diameter either $D = 200$ nm (red curves) or $D = 216$ nm (blue curves), we observe that the width of the lattice resonances supported by these single-particle arrays is significantly smaller than that of the bipartite array with $y_2 = 0$, but larger than the one of the array with $y_2 = a/2$. This is consistent with the increase and decrease of the radiative losses expected, respectively, for a super- and a subradiant mode.

In order to confirm the super- and subradiant nature of the lattice resonances supported by the bipartite arrays with $y_2 = 0$ and $y_2 = a/2$, we perform a detailed analysis of the total dipole induced in the unit cell. Specifically, defining $\beta = 2/(\alpha_1^{-1} + \alpha_2^{-1})$ and $\delta = \alpha_1^{-1} - \alpha_2^{-1}$, we can rewrite $p = p_1 + p_2$ as (see the Methods)

$$p = \frac{\zeta_+ E_0}{\beta^{-1} - \Omega_+} + \frac{\zeta_- E_0}{\beta^{-1} - \Omega_-} \tag{5}$$

where $\zeta_\pm = (\eta \pm 1)/\eta$, $\Omega_\pm = \mathcal{G}_{11} \pm \mathcal{G}_{12}\eta$, and $\eta = \sqrt{1 + \delta^2/(4\mathcal{G}_{12}^2)}$. In principle, this expression predicts the existence of two lattice resonances associated with the cancelation of the denominator of each of the two terms. However, as shown in Figure S2 of the Supporting Information, $\mathrm{Re}\{\mathcal{G}_{12}\} \approx \mathrm{Re}\{\mathcal{G}_{11}\}$ for $y_2 = 0$ and $\mathrm{Re}\{\mathcal{G}_{12}\} \approx -\mathrm{Re}\{\mathcal{G}_{11}\}$ for $y_2 = a/2$. Then, assuming that the two particles in the unit cell have similar sizes, *i.e.*, $|\beta\delta| \ll 1$, we have $\eta \approx 1 + \delta^2/(8\mathcal{G}_{12}^2)$. This means that $\mathrm{Re}\{\Omega_-\}$, for $y_2 = 0$, and $\mathrm{Re}\{\Omega_+\}$, for $y_2 = a/2$, are of order $\mathrm{Re}\{\delta^2/(8\mathcal{G}_{12})\} \ll \mathrm{Re}\{\mathcal{G}_{11}\}$, thus resulting in the vanishing of the contribution of the collective interaction. Therefore, for each array, one of the terms of eq 5 corresponds, approximately, to the localized dipolar plasmon of the nanoparticles and thus only the other one gives rise to a lattice resonance. In other words, the arrays with $y_2 = 0$ and $y_2 = a/2$ support a single lattice resonance associated with the first (Ω_+) and second (Ω_-) terms of eq 5, respectively, both of which appear in the spectrum approximately at wavelengths for which $\mathrm{Re}\{\beta^{-1} - 2\mathcal{G}_{11}\} \approx 0$. These lattice resonances have very different characteristics. First of all, their amplitude is proportional to $\zeta_\pm$, which, for $|\beta\delta| \ll 1$, results in $\zeta_+ \approx 2 + \delta^2/(8\mathcal{G}_{12}^2) \approx 2$ and $\zeta_- \approx \delta^2/(8\mathcal{G}_{12}^2) \ll 1$, respectively. This is what one expects for a super- and subradiant mode. Furthermore, as shown in the Methods, the imaginary part of the denominator of these two terms can be approximated, for $|\beta\delta| \ll 1$, as

$$\mathrm{Im}\{\beta^{-1} - \Omega_\pm\} \approx -\frac{k^3}{3}(\xi_1 + \xi_2) - \frac{2\pi k}{a^2}(1 \pm 1) \mp \mathrm{Im}\left\{\frac{\delta^2}{8\mathcal{G}_{12}}\right\} \tag{6}$$

where $\xi_i = \sigma_i^{\mathrm{abs}}/\sigma_i^{\mathrm{sca}}$ is the ratio between the dipolar absorption, $\sigma_i^{\mathrm{abs}} = 4\pi k(\mathrm{Im}\{\alpha_i\} - 2k^3|\alpha_i|^2/3)$, and scattering, $\sigma_i^{\mathrm{sca}} = 8\pi k^4|\alpha_i|^2/3$, cross sections of particle i. Therefore, the first term on the right-hand side of eq 6 corresponds to the nonradiative losses of the lattice resonance, which are determined by the material and geometrical properties of the nanoparticles (see Figure S3 of the Supporting Information for an analysis of the impact of material properties). The rest of the terms, which depend mostly on the array geometry through the lattice sum, can be interpreted as the radiative losses. As a result, the lattice resonances supported by the bipartite arrays

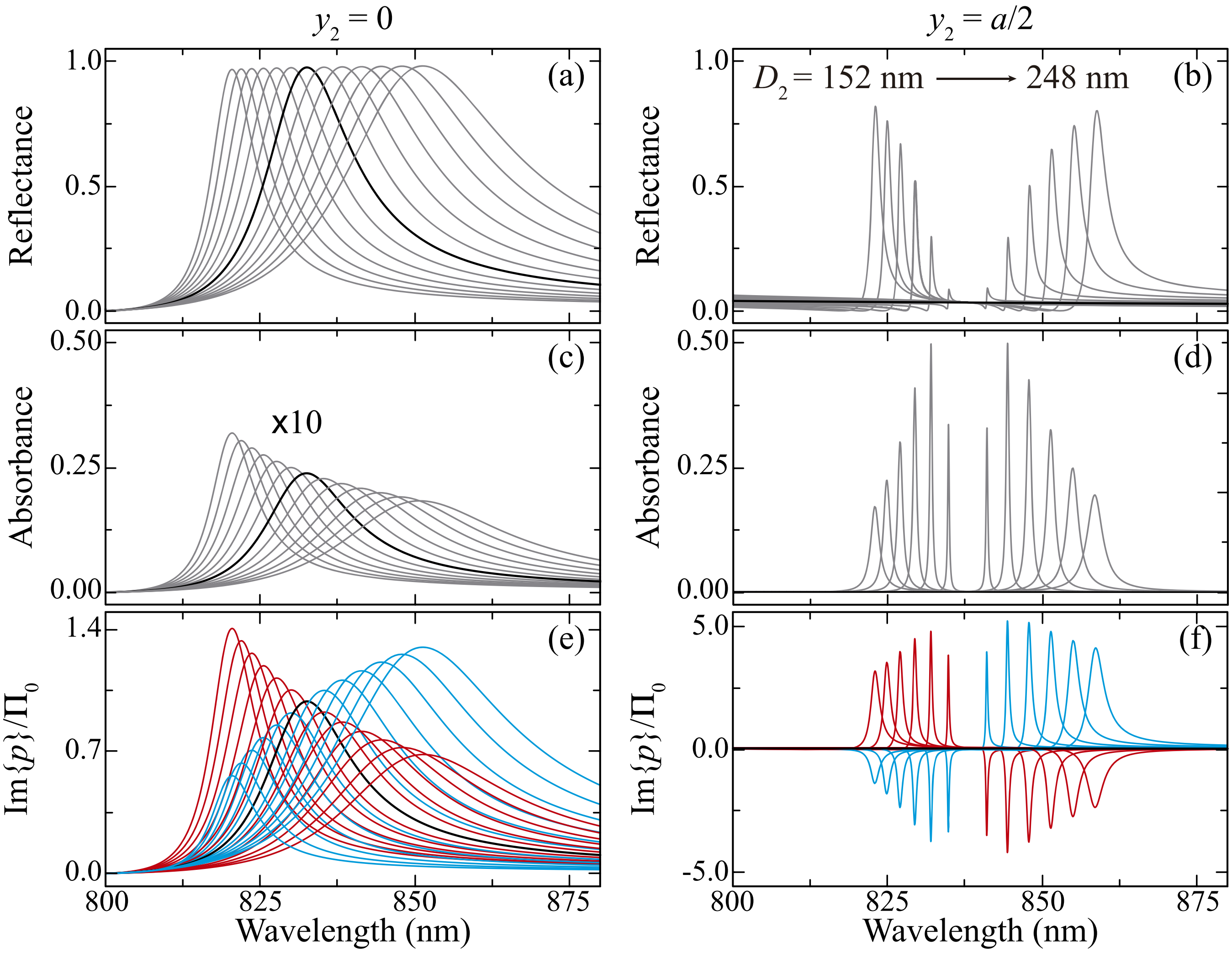

Figure 2. Role of particle size on the super- and subradiant lattice resonances. Spectral dependence of the reflectance (a, b), absorbance (c, d), and imaginary part of the dipole induced in the each of the particles (e, f) for the super- ($y_2 = 0$, left column) and subradiant array ($y_2 = a/2$, right column). We consider arrays with $a = 800$ nm, $D_1 = 200$ nm, and D_2 varying from 152 nm (leftmost curves) to 248 nm (rightmost curves) in steps of 8 nm. In all panels, the black curves denote the case with $D_2 = D_1$. In panels (e) and (f), the red and blue curves correspond, respectively, to the dipoles induced in particles 1 and 2. Note that the results of panel (c) have been multiplied by 10 to improve visibility.

with $y_2 = 0$ and $y_2 = a/2$ have radiative losses proportional to $4\pi k/a^2 + \mathrm{Im}\{\delta^2/(8\mathcal{G}_{12})\}$ and $-\mathrm{Im}\{\delta^2/(8\mathcal{G}_{12})\}$, respectively. Then, comparing these expressions with the corresponding one for a single-particle array, $2\pi k/a^2$ (see the Methods), we conclude that the radiative losses are doubled for the array with $y_2 = 0$ and significantly reduced for the array with $y_2 = a/2$, since $-\mathrm{Im}\{\delta^2/(8\mathcal{G}_{12})\} \ll 2\pi k/a^2$. Again, this is the expected behavior for super- and subradiant modes. Based on this analysis, we conclude that the bipartite arrays with $y_2 = 0$ and $y_2 = a/2$ support a super- and subradiant lattice resonance, respectively.

We can gain further insight into the properties of these lattice resonances by analyzing their dependence with respect to the relative size of the two particles in the unit cell. To that end, in Figures 2a–d, we plot the reflectance and the absorbance of the two bipartite arrays with $y_2 = 0$ (left column) and $y_2 = a/2$ (right column), both of which have $a = 800$ nm and $D_1 = 200$ nm. Each of the curves in these plots corresponds to a different value of D_2, ranging from 152 nm, for the leftmost curve, to 248 nm, for the rightmost one, increasing in steps of 8 nm. As expected from our previous discussion, the superradiant lattice resonances display much broader lineshapes than their subradiant counterparts. Furthermore, for both arrays, the increase of D_2 produces a redshift of the lattice resonance. This behavior can be understood from the condition $\mathrm{Re}\{\beta^{-1} - 2\mathcal{G}_{11}\} \approx 0$, which shifts to larger wavelengths, for which $\mathrm{Re}\{\mathcal{G}_{11}\}$ takes smaller values (see Figure S2 of the Supporting Information), as β^{-1} decreases. However, while the values of the reflectance and absorbance for the superradiant array are not significantly modified with the change of D_2 ($\mathcal{R} \sim 0.98$ and $\mathcal{A} \sim 0.02$ for all values of D_2), the subradiant lattice resonance undergoes dramatic changes as D_2 approaches to D_1. In particular, for $D_2 = D_1$ (black curve), this resonance completely disappears because $\delta = 0$, and therefore, ζ_- vanishes identically. At that point, the subradiant lattice resonance becomes a perfectly dark mode or bound state in the continuum, as recently shown.[86] It is worth noting that all of these results are obtained assuming the arrays are excited at normal incidence. Any deviation from this condition results in a spectral shift of the lattice resonance, which has a stronger impact in the case of the subradiant lattice resonance due to its narrower lineshape, as discussed in Figure S4 of the Supporting Information.

All of these trends are consistent with the behavior of the dipole moment induced in the nanoparticles, which is plotted in panels e and f. There, we use red and blue curves to denote the imaginary part of dipole induced in particles 1 and 2, respectively, with the black curve representing, again, the case $D_1 = D_2$. Expectedly, for the superradiant lattice resonance, the two dipoles oscillate in phase, resulting in a stronger combined dipole moment, which explains the large reflectance values. On the other hand, for the subradiant array, although the dipoles induced in the two particles have larger absolute values, which justifies the larger absorbance, they also have opposite signs. This means that the two dipoles oscillate in antiphase, with the dipole of the smaller particle always pointing in the direction opposite to the field polarization. These results, which are fully consistent with the predictions of a hybridization model,[81] show explicitly that the subradiant nature of the lattice resonance supported by the bipartite array with $y_2 = a/2$ is a consequence of the mutual cancellation of the dipoles induced in the two particles.

Interestingly, as shown in Figure 2d, the absorbance of the subradiant lattice resonance is greatly increased on both sides of the critical condition $D_2 = D_1$. We explore this phenomenon in more detail in Figure 3a, where we plot the value of the reflectance (red) and absorbance (blue) at the wavelength for which the latter is maximum. We use empty and filled dots, respectively, for the super- and subradiant lattice resonances investigated in Figure 2. However, in this case, we vary D_2 in steps of 2 nm for increased resolution. As discussed before, the reflectance and absorbance of the superradiant array remain almost constant as the value of D_2 is varied, whereas, for the subradiant system, we observe significant changes. In particular, the reflectance monotonically decreases as D_2 approaches D_1 from either side. However, the absorbance displays two maxima at $D_2 = 184$ nm and $D_2 = 216$ nm (see the dashed lines). At these points, the absorbance reaches 0.5, which is the theoretical maximum value for a two-dimensional system.[85]

We can understand this behavior by examining the expression of the absorbance given in eq 4. First, to maximize this quantity, the total induced dipole p, which, for convenience, we write as $p = |p|e^{i\varphi}$, must be purely imaginary since any real component only serves to reduce $\mathcal{A}$. With that assumption, and taking the derivative of $\mathcal{A}$ with respect to $|p|$, we find that its maximum is reached at $|p| = \Pi_0$, for which $\mathcal{A} = 0.5$. In other words, the absorbance saturates the theoretical maximum for $p = i\Pi_0$. Interestingly, for that value of p, the reflectance becomes $\mathcal{R} = 0.25$, in complete agreement with the results of previous works.[85] Indeed, noticing that, for a perfectly periodic array, the absorption and scattering efficiencies can be assimilated to $\mathcal{A}$ and $2\mathcal{R}$, respectively, this condition can be seen as a manifestation of the well-known result that states that the maximum absorption of a dipolar system is reached when its absorption and scattering efficiencies become equal.[87,88] In order to verify these arguments, in Figure 3b we plot the magnitude (yellow) and the phase (green) of p for the same systems analyzed in panel a. Again, we use empty and filled dots for the super- and subradiant arrays, respectively. Clearly, the magnitude of p for the subradiant system approaches Π_0 and its phase becomes $\varphi = \pi/2$ for $D_2 = 184$ nm and $D_2 = 216$ nm, in excellent agreement with our predictions. On the other hand, for the superradiant system, the magnitude and phase of p remain at $2\Pi_0$ and $\pi/2$, respectively. This means that, following eq 4, both the reflectance and absorbance are independent of D_2 and take values $\mathcal{R} = 1$ and $\mathcal{A} = 0$, respectively, which is in complete consistency with the results of panel a.

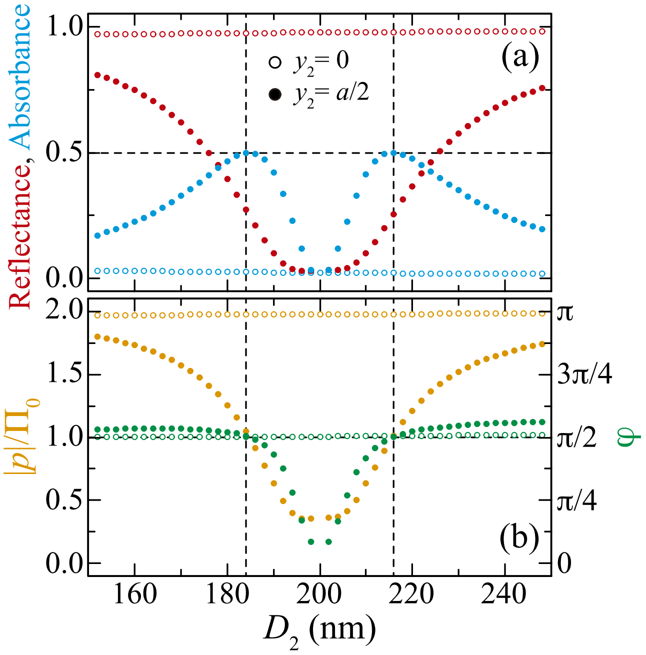

Figure 3. Conditions for maximum absorbance in bipartite nanoparticle arrays. (a) Value of the reflectance (red) and absorbance (blue) for the lattice resonance of the sub- and superradiant arrays, calculated at the wavelength of maximum absorbance as a function of D_2. (b) Normalized magnitude of the total dipole (*i.e.*, $p = p_1 + p_2$) induced in the unit cell (yellow, left scale), and its corresponding phase φ (green, right scale), calculated at the wavelengths of panel (a). In all cases, we consider arrays with $a = 800$ nm and $D_1 = 200$ nm, and vary D_2 from 152 to 248 nm in steps of 2 nm. We use filled dots to display the results for the subradiant array (*i.e.*, $y_2 = a/2$) and empty dots for those corresponding to the superradiant array (*i.e.*, $y_2 = 0$). The vertical dashed lines indicate the two values of D_2 (184 and 216 nm) for which the absorbance of the subradiant array reaches 0.5.

So far, we have focused on bipartite arrays in which the second particle in the unit cell is placed at either $y_2 = 0$ or $y_2 = a/2$. These systems, as shown above, support a single lattice resonance due to the fact that $\mathrm{Re}\{\mathcal{G}_{12}\} \approx \mathrm{Re}\{\mathcal{G}_{11}\}$ for $y_2 = 0$ and $\mathrm{Re}\{\mathcal{G}_{12}\} \approx -\mathrm{Re}\{\mathcal{G}_{11}\}$ for $y_2 = a/2$. However, this is not the expected behavior for arbitrary values of y_2 lying between these two limits. In these cases, eq 5 predicts the existence of two different lattice resonances whose optical properties are largely determined by the interplay between $\mathcal{G}_{12}$ and δ. This is confirmed in Figure 4, where we analyze the spectral position and optical properties of the lattice resonances supported by arrays with arbitrary values of y_2. Specifically, panels a−c and d−f display, respectively, the wavelength of the peaks in the absorbance and reflectance spectra as a function of y_2. We consider arrays with $a = 800$ nm, $D_1 = 200$ nm, and different values of D_2 as indicated in the labels. In all cases, the area of the circles is proportional to the value of the absorbance or reflectance at the corresponding peak, while their color encodes the function $\chi = |p_1 - p_2|/|p_1 + p_2|$. This function serves to characterize the nature of the lattice resonance, since

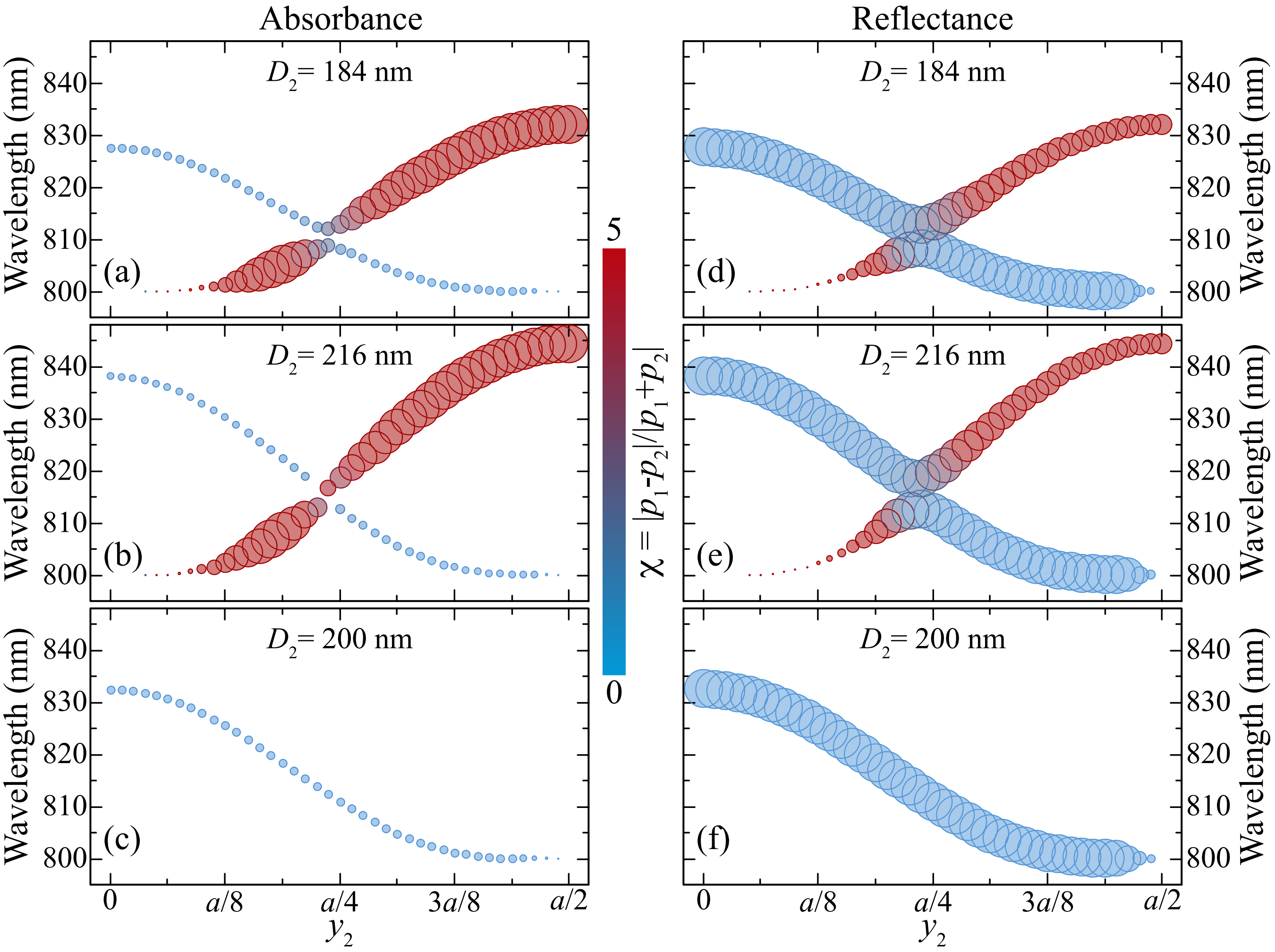

Figure 4. Transition from super- to subradiant lattice resonances in bipartite nanoparticle arrays. We plot the wavelength of the absorbance (a−c) and reflectance (d−f) peaks as a function of y_2. The area of the circles is proportional to the corresponding value of the absorbance or the reflectance at that wavelength, while their color encodes the function $\chi = |p_1 - p_2|/|p_1 + p_2|$, following the scale in the middle. In all cases, we consider arrays with a = 800 nm and D_1 = 200 nm, whereas the value of D_2 is, respectively, 184, 216, and 200 nm for panels (a, d), (b, e), and (c, f).

its value ranges from zero for a perfectly superradiant mode with $p_1 = p_2$ to large numbers for subradiant modes, for which $p_1 \approx - p_2$.

Exploring the results plotted in Figure 4, we observe that, for the two cases with $D_1 \neq D_2$, there are two lattice resonances whose spectral positions coalesce as the value y_2 approaches $a/4$. This can be understood by noticing that, as shown in Figure S2 of the Supporting Information, $\mathrm{Re}\{\mathcal{G}_{12}\} \ll \mathrm{Re}\{\mathcal{G}_{11}\}$ for $y_2 = a/4$, which results in Ω_+ and Ω_- having similar values. It is worth mentioning that the wavelengths of the peaks of the absorbance and reflectance spectrum do not exactly coincide, which is consistent with the fact that the reflectance is directly proportional to $|p|^2$ while the absorbance depends on the interplay between $\mathrm{Im}\{p\}$ and $|p|^2$, as shown in eq 4. Interestingly, the results of panels a, b and d, e show that, for values of y_2 below $a/4$, the lattice resonance located at longer wavelengths has a superradiant character, as inferred from the large reflectance and the vanishing value of χ. On the other hand, the lattice resonance closer to the Rayleigh anomaly (*i.e.*, $\lambda = a$) exhibits large values of absorbance and χ, thus corresponding to a subradiant mode. This trend is completely reversed for y_2 above $a/4$. In this case, the resonance appearing at longer wavelengths displays the subradiant character, while the one at shorter wavelengths corresponds to the superradiant mode. As expected from the analysis of eq 5, the subradiant mode becomes completely dark and hence disappears from both the absorbance and reflectance spectra when the two particles are identical (*i.e.*, $D_1 = D_2$).

A distinct feature of the lattice resonance supported by the subradiant bipartite array is its reduced lineshape as compared with its superradiant counterpart. Consequently, the subradiant lattice resonance displays a much larger quality factor Q, as shown in Figure 5a. There, we use green and yellow dots, respectively, to plot Q for the super- and subradiant arrays as a function of D_2. We consider systems with a = 800 nm and D_1 = 200 nm, and vary D_2 from 152 to 248 nm, in steps of 2 nm, as in Figure 3. For simplicity, and to enable a later comparison with finite arrays, we always calculate the quality factor from the spectrum of the extinction efficiency. For infinite arrays, within the dipolar approximation, this quantity is defined as $\mathcal{E} = \mathrm{Im}\{p\}/\Pi_0$ (see the Methods). Examining the results of Figure 5a, we observe that the quality factor of the superradiant lattice resonance is always below 100 for the values of D_2

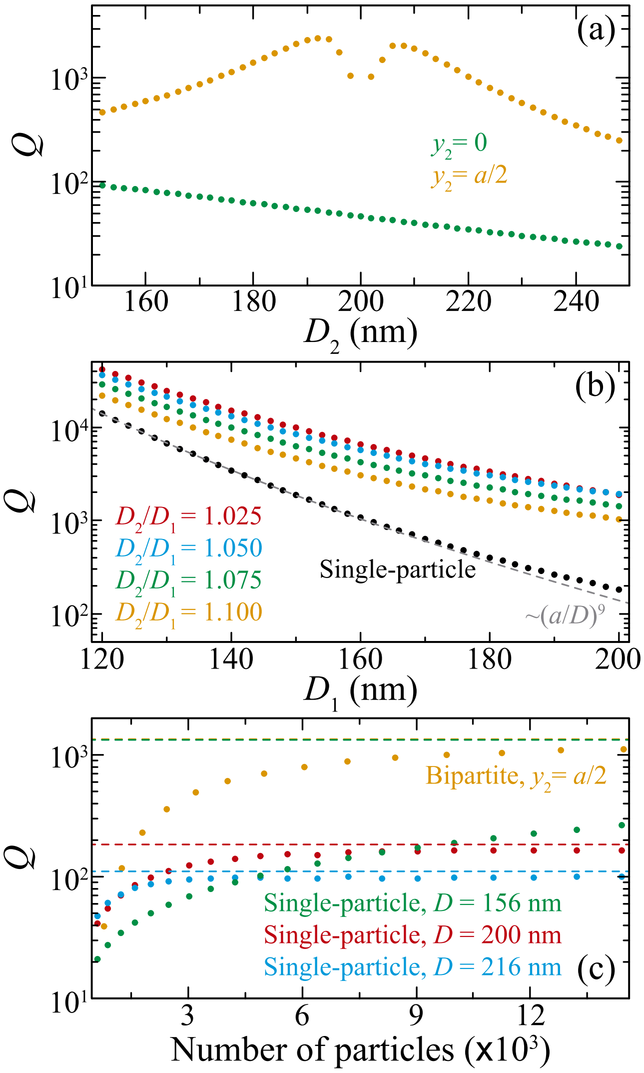

Figure 5. Analysis of the quality factor of the lattice resonances. (a) Quality factor for the lattice resonance of the super- and subradiant arrays, plotted as a function of D_2. We assume D_1 = 200 nm and use green (yellow) dots to display the results for the array with $y_2 = 0$ ($y_2 = a/2$). (b) Quality factor for the lattice resonance of the subradiant array plotted as a function of D_1 for different ratios D_2/D_1, as indicated in the legend. For comparison, we plot the results for a single-particle array with $D = D_1$ using black dots. The dashed gray line indicates a scaling of $\sim(a/D)^9$. (c) Analysis of the convergence to the infinite array limit. The yellow dots show Q for the lattice resonance of a subradiant array (*i.e.*, $y_2 = a/2$) with a finite number of particles, as indicated by the horizontal axis. The array has D_1 = 200 nm and D_2 = 216 nm. For comparison, we plot Q for a single-particle array with D = 156 nm (green dots), D = 200 nm (red dots), and D = 216 nm (blue dots). The dashed lines represent the value of Q for the corresponding infinite array. As in the rest of the paper, we assume a = 800 nm for all the arrays.

analyzed. On the contrary, for the subradiant lattice resonance, Q is beyond 1000 for D_2 in the range 174−220 nm, reaching two local maxima of ∼2400 for D_2 = 192 nm and ∼2000 for D_2 = 208 nm. Interestingly, these values of D_2 are not far from the ones that maximized the absorbance, D_2 = 184 nm and D_2 = 216 nm, for which Q is ∼1700 and ∼1300, respectively.

Importantly, as we show below, the quality factor of the subradiant bipartite array is also larger than that of a single-particle array with similar period and particle size. In a previous work,[38] we demonstrated that the quality factor of the lattice resonance of a single-particle array with period a and particle size D scales as $Q \sim (\lambda_{\mathrm{LR}}/a - 1)^{-3/2}$ in the limit $D \ll a$. In this expression, λ_{LR} is the lattice resonance wavelength, which, in the same limit, satisfies $\lambda_{\mathrm{LR}}/a - 1 \sim (D/a)^6$, thus resulting in $Q \sim (a/D)^9$ (see the Methods for more details). Therefore, by using single-particle arrays with decreasing D/a, it is possible to obtain lattice resonances with increasingly large quality factors.[40] This can be seen in Figure 5b, where the black dots represent the value of Q for the lattice resonance of a single-particle array with period a = 800 nm and particle diameter $D = D_1$.

However, for a given value of D_1, it is possible to construct a subradiant bipartite array supporting a lattice resonance with a Q larger than that of a single-particle array with the same periodicity. See, for instance, the yellow dots in Figure 5b, which show the quality factor for the lattice resonance of a subradiant array with D_2/D_1 = 1.100. By decreasing this ratio, it is possible to further increase the quality factor, as shown by the other colored dots. Interestingly, for the largest sizes under consideration, all of the ratios D_2/D_1 result in a value of Q that is almost 1 order of magnitude larger than that of the single-particle array. However, as D_1 decreases, it is necessary to use an increasingly smaller ratio to see the same improvement.

It is important to remark that all of the results discussed so far are based on calculations for infinite arrays. However, in a practical implementation, the arrays necessarily have a finite size. This imposes some important limitations on the actual performance of these systems.[89−94] For instance, although, as explained above, the quality factor of a single-particle array can be made arbitrarily large by decreasing the ratio D/a, this requires, in practice, an increasingly large system. The reason is that, following eq 3, the decrease of D/a results in a smaller particle polarizability and thus a larger $\mathrm{Re}\{\alpha^{-1}\}$, which, in turn, demands a larger value of the lattice sum $\mathrm{Re}\{\mathcal{G}_{11}\}$, as discussed in our previous work.[38] For an infinite array, it is possible to obtain an arbitrarily large value of $\mathrm{Re}\{\mathcal{G}_{11}\}$, since the value of this quantity diverges at the Rayleigh anomaly, that is, as λ approaches a from the red side (see Figure S2 in the Supporting Information). However, for a finite array, the value of $\mathrm{Re}\{\mathcal{G}_{11}\}$ is constrained by the number of particles in the array that can coherently interact, which, in a practical implementation, is obviously limited by the size of the array.

Interestingly, from the discussion of eq 5, we concluded that the lattice resonance of the subradiant bipartite array appears at wavelengths for which $\mathrm{Re}\{\beta^{-1} - 2\mathcal{G}_{11}\} \approx 0$. Since $\beta^{-1} = (\alpha_1^{-1} + \alpha_2^{-1})/2$ and, for the systems under investigation, $\alpha_1 \approx \alpha_2$, this means that this subradiant resonance requires a value of $\mathrm{Re}\{\mathcal{G}_{11}\}$ that is effectively half of the value necessary for the lattice resonance of the single-particle array. Therefore, for similar periodicity and particle size, the subradiant bipartite array is expected to be more robust to finite-size effects than a single-particle array, thus requiring a smaller number of elements to reach the infinite array limit. Incidentally, for the same reason, the lattice resonance of the subradiant bipartite array is also expected to be more robust to inhomogeneities in the dielectric environment surrounding the array. When large enough, such inhomogeneities have been shown to hinder the collective interactions between the elements of the array, suppressing the lattice resonances of the system.[95]

In Figure 5c, we analyze the quality factor for different finite arrays as a function of their total number of elements. In all cases, we consider arrays with a period a = 800 nm and, as in panels a and b, calculate Q from the extinction efficiency. This quantity is given, for a finite array with N particles and $\mathcal{N}$ unit cells under normal illumination, by $\mathcal{E} = \sum_{i=1}^{N} \mathrm{Im}\{P_i\}/(\mathcal{N}\Pi_0)$, where P_i represents the self-consistent dipole moment induced in particle i of the finite array[92] (see the Methods). The yellow dots in Figure 5c represent the value of Q for a finite subradiant bipartite array (*i.e.*, $y_2 = a/2$), with D_1 = 200 nm and D_2 = 216 nm. Examining the results, we observe that, for N = 7200, Q has already reached ∼66% of the value of the corresponding infinite array, which is indicated by the dashed line of the same color. This is in sharp contrast with the behavior of a single-particle array with D = 156 nm, whose results are shown by the green dots. We chose this particular value of D because it results in practically the same Q as the subradiant bipartite array in the infinite array limit (notice the overlapping green and yellow dashed lines). However, for a similar number of particles (N = 7225), the quality factor of this array is only 11% of the infinite array limit, thus confirming our predictions. To complete our analysis, we also plot the evolution of Q for another two single-particle arrays with D = 200 nm (red dots) and D = 216 nm (blue dots). The larger particle diameter makes these systems converge faster to the infinite array limit but, at the same time, results in a drastic reduction of the value of Q as compared with the subradiant bipartite array. All of these results demonstrate that the lattice resonance of a subradiant bipartite array is more robust to finite-size effects than those supported by single-particle arrays with similar dimensions.

CONCLUSIONS

In summary, we have provided a comprehensive analysis of the lattice resonances supported by bipartite nanoparticle arrays. Using a rigorous coupled dipole model, we have shown that it is possible to obtain lattice resonances with either a super- or subradiant character, depending on the relative position of the two particles within the unit cell, which exhibit very different optical responses. In particular, superradiant lattice resonances are characterized by the dipole moments of the two particles oscillating in phase, thus resulting in increased radiative losses that lead to large reflectance values and broad lineshapes. In sharp contrast with this, subradiant lattice resonances display much narrower lineshapes, and therefore much higher quality factors, as well as large values of the absorbance, all of which are consistent with the decrease of the radiative losses caused by the partial cancellation of the dipoles induced in the two particles. In addition, we have found that, while the relative size of the two particles has a minimal impact on the response of the superradiant array, the optical response of the subradiant one undergoes a dramatic transformation as the particle size is changed, making it possible to reach perfect absorbance while maintaining large quality factors. Furthermore, we have demonstrated that the lattice resonance of a subradiant bipartite array is more robust to finite-size effects than the lattice resonance supported by a single-particle array with similar period and particle size and, therefore, a subradiant bipartite array requires a smaller number of elements to achieve a given quality factor. Our results shed light on the optical response of bipartite arrays of nanoparticles and provide a simple path to achieve lattice resonances with large quality factors that are robust to finite-size effects and, therefore, fabrication imperfections.

METHODS

Derivation of eqs 2–6 Using the Coupled Dipole Model. Thanks to the periodicity of the array, eq 1 can be rewritten in terms of Bloch waves as $p_i = \alpha_i\left[E_0 + \sum_{j=1}^{2} \mathcal{G}_{ij} p_j\right]$, where p_i represents the amplitude of the dipole induced in the particle i of every unit cell.[27,38,81] The explicit solution of this equation,

$$\begin{bmatrix} p_1 \\ p_2 \end{bmatrix} = \begin{bmatrix} \alpha_1^{-1} - \mathcal{G}_{11} & -\mathcal{G}_{12} \\ -\mathcal{G}_{12} & \alpha_2^{-1} - \mathcal{G}_{11} \end{bmatrix}^{-1} \begin{bmatrix} E_0 \\ E_0 \end{bmatrix}$$

leads directly to eq 2. Notice that, here, we have used the fact that $\mathcal{G}_{22} = \mathcal{G}_{11}$ and $\mathcal{G}_{21} = \mathcal{G}_{12}$. The total dipole induced in the unit cell can then be written as

$$p = p_1 + p_2 = \frac{\alpha_1^{-1} + \alpha_2^{-1} + 2(\mathcal{G}_{12} - \mathcal{G}_{11})}{(\alpha_1^{-1} - \mathcal{G}_{11})(\alpha_2^{-1} - \mathcal{G}_{11}) - \mathcal{G}_{12}^2} E_0$$

which clearly reduces to the usual result for a single-particle array given in eq 3 when one of the particles is removed from the unit cell. Following simple algebraic manipulations, the expression above can be split into the two terms of eq 5.

Once the total dipole induced in the unit cell is known, we can calculate the reflectance, transmittance, and absorbance of the array from the field that it scatters. For the illumination conditions used in our investigation, and assuming $\lambda > a$, all of the diffracted beams except the zero-order are evanescent and consequently vanish in the far-field. Therefore, the amplitude of the scattered field can be simply written as $E_{\mathrm{sca}} = 2\pi i k p/a^2$.[27,38,81] Using this result, the total intensity reflected by the array is given by $I_{\mathcal{R}} = c|E_{\mathrm{sca}}|^2/(2\pi)$, while the total intensity transmitted reads $I_{\mathcal{T}} = c[E_0^2 + |E_{\mathrm{sca}}|^2 + 2E_0\mathrm{Re}\{E_{\mathrm{sca}}\}]/(2\pi)$. Then, the reflectance, transmittance, and absorbance of the array are $\mathcal{R} = I_{\mathcal{R}}/I_0$, $\mathcal{T} = I_{\mathcal{T}}/I_0$, and $\mathcal{A} = 1 - \mathcal{R} - \mathcal{T}$, with $I_0 = cE_0^2/(2\pi)$ being the incident intensity. Simplifying these expressions, we obtain eq 4.

Finally, to derive eq 6, we need to compute the imaginary parts of β^{-1} and $\Omega_\pm$. The former is given by

$$\mathrm{Im}\{\beta^{-1}\} = -\frac{\mathrm{Im}\{\alpha_1\}}{2|\alpha_1|^2} - \frac{\mathrm{Im}\{\alpha_2\}}{2|\alpha_2|^2} = -\frac{k^3}{3}(\xi_1 + \xi_2) - \frac{2k^3}{3}$$

where ξ_1 and ξ_2 are ratios between the dipolar absorption and scattering cross sections for particles 1 and 2 defined in the main text. Moreover, for $\lambda > a$, we can use the Weyl identity[6] to obtain $\mathrm{Im}\{\mathcal{G}_{ij}\} = 2\pi k/a^2 - 2k^3\delta_{ij}/3$ (with δ_{ij} being the Kronecker delta function), as shown in ref 81. Therefore,

$$\mathrm{Im}\{\beta^{-1} - \Omega_\pm\} = -\frac{k^3}{3}(\xi_1 + \xi_2) - \frac{2\pi k}{a^2} \mp \mathrm{Im}\{\mathcal{G}_{12}\eta\}$$

Then, taking the limit of $|\beta\delta| \ll 1$, in which $\eta \approx 1 + \delta^2/(8\mathcal{G}_{12}^2)$, this expression reduces to eq 6.

Quality Factor of a Single-Particle Unit Cell Array. As demonstrated in ref 38, the quality factor of the first lattice resonance supported by a single particle array scales as

$$Q \sim \left(\frac{\lambda_{\mathrm{LR}}}{a} - 1\right)^{-3/2}$$

in the limit in which the period of the array, a, is much larger than the particle size D. Here, λ_{LR} is the wavelength of the lattice resonance, which is approximately defined by the condition $\mathrm{Re}\{\alpha^{-1} - \mathcal{G}_{11}\} \approx 0$. Away from the localized plasmon resonance of the particle $\mathrm{Re}\{\alpha^{-1}\} \sim D^{-3}$, while, as shown in refs 27 and 38, $\mathrm{Re}\{\mathcal{G}_{11}\} \sim a^{-3}(\lambda/a - 1)^{-1/2}$. Therefore, $(\lambda_{\mathrm{LR}}/a - 1) \sim (D/a)^6$, which allows us to finally write

$Q \sim (a/D)^9$. The validity of this scaling is confirmed by the gray dashed line in Figure 5b.

Extinction Efficiency for Infinite and Finite Arrays. The extinction efficiency allows us to compare the properties of infinite and finite arrays in a consistent way. For a finite square array with N particles and $\mathcal{N}$ unit cells, under the illumination conditions used throughout this work, this quantity is defined as

$$\mathcal{E} = \frac{4\pi k}{\mathcal{N} a^2 E_0}\sum_{i=1}^{N}\mathrm{Im}\{P_i\} = \frac{1}{\mathcal{N}\Pi_0}\sum_{i=1}^{N}\mathrm{Im}\{P_i\}$$

Here, P_i represents the x-component of the self-consistent dipole induced in particle i of the finite array, which is obtained from the self-consistent solution of

$$\mathbf{P}_i = \alpha_i E_0 \hat{\mathbf{x}} + \alpha_i \sum_{j=1}^{N}\mathbf{G}_{ij}\mathbf{P}_j$$

with $\mathbf{G}_{ij} = [k^2 + \nabla\nabla] e^{ik|\mathbf{r}_i - \mathbf{r}_j|}/|\mathbf{r}_i - \mathbf{r}_j|$ being the dipole−dipole interaction tensor that describes the coupling between the dipoles of particles i and j. Similarly, for an infinite array, this quantity is defined as

$$\mathcal{E} = \frac{4\pi k}{a^2 E_0}\sum_{i=1}^{2}\mathrm{Im}\{p_i\} = \frac{\mathrm{Im}\{p\}}{\Pi_0}$$

where now p_i is the amplitude of the Bloch wave describing the dipole induced in the particle i of every unit cell in the array.

ASSOCIATED CONTENT

Supporting Information

The Supporting Information is available free of charge at https://pubs.acs.org/doi/10.1021/acsnano.0c04795.

> Comparison of the coupled dipole model with rigorous solutions of Maxwell's equations, obtained using a finite element method approach; analysis of the real part of the lattice sums for the bipartite arrays; analysis of the effect of the material properties and the angle of incidence on the lattice resonances supported by bipartite arrays (PDF)

AUTHOR INFORMATION

Corresponding Author

Alejandro Manjavacas − *Department of Physics and Astronomy, University of New Mexico, Albuquerque, New Mexico 87106, United States;* orcid.org/0000-0002-2379-1242; Email: manjavacas@unm.edu

Authors

Alvaro Cuartero-González − *Departamento de Física Teórica de la Materia Condensada and Condensed Matter Physics Center (IFIMAC), Universidad Autónoma de Madrid, E-28049 Madrid, Spain*

Stephen Sanders − *Department of Physics and Astronomy, University of New Mexico, Albuquerque, New Mexico 87106, United States*

Lauren Zundel − *Department of Physics and Astronomy, University of New Mexico, Albuquerque, New Mexico 87106, United States;* orcid.org/0000-0003-1850-5210

Antonio I. Fernández-Domínguez − *Departamento de Física Teórica de la Materia Condensada and Condensed Matter Physics Center (IFIMAC), Universidad Autónoma de Madrid, E-28049 Madrid, Spain;* orcid.org/0000-0002-8082-395X

Complete contact information is available at:
https://pubs.acs.org/10.1021/acsnano.0c04795

Notes

The authors declare no competing financial interest.

ACKNOWLEDGMENTS

This work has been sponsored by the U.S. National Science Foundation (Grant No. ECCS-1710697). We thank the UNM Center for Advanced Research Computing, supported in part by the U.S. National Science Foundation, for providing the computational resources used in this work. L.Z. acknowledges support from the New Mexico Space Grant Consortium and the Department of Energy Computational Science Graduate Fellowship (Grant No. DE-SC0020347). A.C.-G. and A.I.F.-D. acknowledge funding from Spanish MINECO Contract No. MDM-2014-0377-16-4 and from the Spanish Ministry for Science and Innovation under Contract No. RTI2018-099737-B-I00 and through the "María de Maeztu" programme for Units of Excellence in R&D (CEX2018-000805-M).

REFERENCES

(1) Maier, S. A. *Plasmonics: Fundamentals and Applications*; Springer: New York, 2007.

(2) Álvarez-Puebla, R. A.; Liz-Marzán, L. M.; García de Abajo, F. J. Light Concentration at the Nanometer Scale. *J. Phys. Chem. Lett.* **2010**, *1*, 2428−2434.

(3) Atwater, H. A.; Polman, A. Plasmonics for Improved Photovoltaic Devices. *Nat. Mater.* **2010**, *9*, 205−213.

(4) Brongersma, M. L.; Halas, N. J.; Nordlander, P. Plasmon-Induced Hot Carrier Science and Technology. *Nat. Nanotechnol.* **2015**, *10*, 25−34.

(5) Rastinehad, A. R.; Anastos, H.; Wajswol, E.; Winoker, J. S.; Sfakianos, J. P.; Doppalapudi, S. K.; Carrick, M. R.; Knauer, C. J.; Taouli, B.; Lewis, S. C.; Tewari, A. K.; Schwartz, J. A.; Canfield, S. E.; George, A. K.; West, J. L.; Halas, N. J. Gold Nanoshell-Localized Photothermal Ablation of Prostate Tumors in a Clinical Pilot Device Study. *Proc. Natl. Acad. Sci. U. S. A.* **2019**, *116*, 18590−18596.

(6) Novotny, L.; Hecht, B. *Principles of Nano-Optics*; Cambridge University Press: New York, 2006.

(7) Derom, S.; Vincent, R.; Bouhelier, A.; Colas des Francs, G. Resonance Quality, Radiative/Ohmic Losses and Modal Volume of Mie Plasmons. *Europhys. Lett.* **2012**, *98*, 47008.

(8) Doiron, B.; Mota, M.; Wells, M. P.; Bower, R.; Mihai, A.; Li, Y.; Cohen, L. F.; Alford, N. M.; Petrov, P. K.; Oulton, R. F.; Maier, S. A. Quantifying Figures of Merit for Localized Surface Plasmon Resonance Applications: A Materials Survey. *ACS Photonics* **2019**, *6*, 240−259.

(9) Anker, J. N.; Hall, W. P.; Lyandres, O.; Shah, N. C.; Zhao, J.; Van Duyne, R. P. Biosensing with Plasmonic Nanosensors. *Nat. Mater.* **2008**, *7*, 442−453.

(10) Lozano, G.; Louwers, D. J.; Rodríguez, S. R. K.; Murai, S.; Jansen, O. T. A.; Verschuuren, M. A.; Gómez Rivas, J. Plasmonics for Solid-State Lighting: Enhanced Excitation and Directional Emission of Highly Efficient Light Sources. *Light: Sci. Appl.* **2013**, *2*, No. 66.

(11) Nordlander, P.; Oubre, C.; Prodan, E.; Li, K.; Stockman, M. I. Plasmon Hybridization in Nanoparticle Dimers. *Nano Lett.* **2004**, *4*, 899−903.

(12) Chu, M. W.; Myroshnychenko, V.; Chen, C. H.; Deng, J. P.; Mou, C. Y.; García de Abajo, F. J. Probing Bright and Dark Surface-Plasmon Modes in Individual and Coupled Noble Metal Nanoparticles Using an Electron Beam. *Nano Lett.* **2009**, *9*, 399−404.

(13) Koh, A. L.; Bao, K.; Khan, I.; Smith, W. E.; Kothleitner, G.; Nordlander, P.; Maier, S. A.; McComb, D. W. Electron Energy-Loss Spectroscopy (EELS) of Surface Plasmons in Single Silver Nanoparticles and Dimers: Influence of Beam Damage and Mapping of Dark Modes. *ACS Nano* **2009**, *3*, 3015−3022.

(14) Sonnefraud, Y.; Verellen, N.; Sobhani, H.; Vandenbosch, G. A.; Moshchalkov, V. V.; Van Dorpe, P.; Nordlander, P.; Maier, S. A. Experimental Realization of Subradiant, Superradiant, and Fano

Resonances in Ring/Disk Plasmonic Nanocavities. *ACS Nano* **2010**, *4*, 1664−1670.

(15) Lassiter, J. B.; Sobhani, H.; Fan, J. A.; Kundu, J.; Capasso, F.; Nordlander, P.; Halas, N. J. Fano Resonances in Plasmonic Nanoclusters: Geometrical and Chemical Tunability. *Nano Lett.* **2010**, *10*, 3184−3189.

(16) Deng, T.-S.; Parker, J.; Yifat, Y.; Shepherd, N.; Scherer, N. F. Dark Plasmon Modes in Symmetric Gold Nanoparticle Dimers Illuminated by Focused Cylindrical Vector Beams. *J. Phys. Chem. C* **2018**, *122*, 27662−27672.

(17) Hao, F.; Nordlander, P.; Sonnefraud, Y.; Dorpe, P. V.; Maier, S. A. Tunability of Subradiant Dipolar and Fano-Type Plasmon Resonances in Metallic Ring/Disk Cavities: Implications for Nanoscale Optical Sensing. *ACS Nano* **2009**, *3*, 643−652.

(18) Verellen, N.; Van Dorpe, P.; Huang, C.; Lodewijks, K.; Vandenbosch, G. A. E.; Lagae, L.; Moshchalkov, V. V. Plasmon Line Shaping Using Nanocrosses for High Sensitivity Localized Surface Plasmon Resonance Sensing. *Nano Lett.* **2011**, *11*, 391−397.

(19) Gómez, D. E.; Teo, Z. Q.; Altissimo, M.; Davis, T. J.; Earl, S.; Roberts, A. The Dark Side of Plasmonics. *Nano Lett.* **2013**, *13*, 3722−3728.

(20) Sobhani, A.; Manjavacas, A.; Cao, Y.; McClain, M. J.; García de Abajo, F. J.; Nordlander, P.; Halas, N. J. Pronounced Linewidth Narrowing of an Aluminum Nanoparticle Plasmon Resonance by Interaction with an Aluminum Metallic Film. *Nano Lett.* **2015**, *15*, 6946−6951.

(21) Luk'yanchuk, B.; Zheludev, N. I.; Maier, S. A.; Halas, N. J.; Nordlander, P.; Giessen, H.; Chong, C. The Fano Resonance in Plasmonic Nanostructures and Metamaterials. *Nat. Mater.* **2010**, *9*, 707−715.

(22) Miroshnichenko, A. E.; Flach, S.; Kivshar, Y. S. Fano Resonances in Nanoscale Structures. *Rev. Mod. Phys.* **2010**, *82*, 2257.

(23) Giannini, V.; Francescato, Y.; Amrania, H.; Phillips, C. C.; Maier, S. A. Fano Resonances in Nanoscale Plasmonic Systems: A Parameter-Free Modeling Approach. *Nano Lett.* **2011**, *11*, 2835−2840.

(24) Wu, C.; Khanikaev, A. B.; Adato, R.; Arju, N.; Yanik, A. A.; Altug, H.; Shvets, G. Fano-Resonant Asymmetric Metamaterials for Ultrasensitive Spectroscopy and Identification of Molecular Monolayers. *Nat. Mater.* **2012**, *11*, 69−75.

(25) Zhao, L.; Kelly, K. L.; Schatz, G. C. The Extinction Spectra of Silver Nanoparticle Arrays: Influence of Array Structure on Plasmon Resonance Wavelength and Width. *J. Phys. Chem. B* **2003**, *107*, 7343−7350.

(26) Zou, S.; Janel, N.; Schatz, G. C. Silver Nanoparticle Array Structures that Produce Remarkably Narrow Plasmon Lineshapes. *J. Chem. Phys.* **2004**, *120*, 10871−10875.

(27) García de Abajo, F. J. Light Scattering by Particle and Hole Arrays. *Rev. Mod. Phys.* **2007**, *79*, 1267−1290.

(28) Auguié, B.; Barnes, W. L. Collective Resonances in Gold Nanoparticle Arrays. *Phys. Rev. Lett.* **2008**, *101*, 143902.

(29) Kravets, V. G.; Schedin, F.; Grigorenko, A. N. Extremely Narrow Plasmon Resonances Based on Diffraction Coupling of Localized Plasmons in Arrays of Metallic Nanoparticles. *Phys. Rev. Lett.* **2008**, *101*, 087403.

(30) Chu, Y.; Schonbrun, E.; Yang, T.; Crozier, K. B. Experimental Observation of Narrow Surface Plasmon Resonances in Gold Nanoparticle Arrays. *Appl. Phys. Lett.* **2008**, *93*, 181108.

(31) Vecchi, G.; Giannini, V.; Gómez Rivas, J. Surface Modes in Plasmonic Crystals Induced by Diffractive Coupling of Nanoantennas. *Phys. Rev. B: Condens. Matter Mater. Phys.* **2009**, *80*, No. 201401.

(32) Adato, R.; Yanik, A. A.; Wu, C.-H.; Shvets, G.; Altug, H. Radiative Engineering of Plasmon Lifetimes in Embedded Nanoantenna Arrays. *Opt. Express* **2010**, *18*, 4526−4537.

(33) Zakomirnyi, V. I.; Rasskazov, I. L.; Gerasimov, V. S.; Ershov, A. E.; Polyutov, S. P.; Karpov, S. V. Refractory Titanium Nitride Two-Dimensional Structures with Extremely Narrow Surface Lattice Resonances at Telecommunication Wavelengths. *Appl. Phys. Lett.* **2017**, *111*, 123107.

(34) Khlopin, D.; Laux, F.; Wardley, W. P.; Martin, J.; Wurtz, G. A.; Plain, J.; Bonod, N.; Zayats, A. V.; Dickson, W.; Gérard, D. Lattice Modes and Plasmonic Linewidth Engineering in Gold and Aluminum Nanoparticle Arrays. *J. Opt. Soc. Am. B* **2017**, *34*, 691−700.

(35) Wang, W.; Ramezani, M.; Väkeväinen, A. I.; Törmä, P.; Gómez Rivas, J.; Odom, T. W. The Rich Photonic World of Plasmonic Nanoparticle Arrays. *Mater. Today* **2018**, *21*, 303−314.

(36) Kravets, V. G.; Kabashin, A. V.; Barnes, W. L.; Grigorenko, A. N. Plasmonic Surface Lattice Resonances: A Review of Properties and Applications. *Chem. Rev.* **2018**, *118*, 5912−5951.

(37) Le-Van, Q.; Zoethout, E.; Geluk, E.-J.; Ramezani, M.; Berghuis, M.; Gómez Rivas, J. Enhanced Quality Factors of Surface Lattice Resonances in Plasmonic Arrays of Nanoparticles. *Adv. Opt. Mater.* **2019**, *7*, 1801451.

(38) Manjavacas, A.; Zundel, L.; Sanders, S. Analysis of the Limits of the Near-Field Produced by Nanoparticle Arrays. *ACS Nano* **2019**, *13*, 10682−10693.

(39) Zhu, X.; Imran Hossain, G. M.; George, M.; Farhang, A.; Cicek, A.; Yanik, A. A. Beyond Noble Metals: High Q-Factor Aluminum Nanoplasmonics. *ACS Photonics* **2020**, *7*, 416−424.

(40) Bin-Alam, M. S.; Reshef, O.; Mamchur, Y.; Alam, M. Z.; Carlow, G.; Upham, J.; Sullivan, B. T.; Ménard, J.-M.; Huttunen, M. J.; Boyd, R. W.; Dolgaleva, K. Ultra-High-Q Resonances in Plasmonic Metasurfaces. *arXiv* 2020, 05202. https://arxiv.org/abs/2004.05202 (accessed 2020-05-12).

(41) Rodriguez, S. R. K.; Lozano, G.; Verschuuren, M. A.; Gomes, R.; Lambert, K.; Geyter, B. D.; Hassinen, A.; Thourhout, D. V.; Hens, Z.; Rivas, J. G. Quantum Rod Emission Coupled to Plasmonic Lattice Resonances: A Collective Directional Source of Polarized Light. *Appl. Phys. Lett.* **2012**, *100*, 111103.

(42) Zhou, W.; Dridi, M.; Suh, J. Y.; Kim, C. H.; Co, D. T.; Wasielewski, M. R.; Schatz, G. C.; Odom, T. W. Lasing Action in Strongly Coupled Plasmonic Nanocavity Arrays. *Nat. Nanotechnol.* **2013**, *8*, 506−511.

(43) Lozano, G.; Grzela, G.; Verschuuren, M. A.; Ramezani, M.; Rivas, J. G. Tailor-Made Directional Emission in Nanoimprinted Plasmonic-Based Light-Emitting Devices. *Nanoscale* **2014**, *6*, 9223−9229.

(44) Schokker, A. H.; Koenderink, A. F. Lasing at the Band Edges of Plasmonic Lattices. *Phys. Rev. B: Condens. Matter Mater. Phys.* **2014**, *90*, 155452.

(45) Ramezani, M.; Lozano, G.; Verschuuren, M. A.; Gómez-Rivas, J. Modified Emission of Extended Light Emitting Layers by Selective Coupling to Collective Lattice Resonances. *Phys. Rev. B: Condens. Matter Mater. Phys.* **2016**, *94*, 125406.

(46) Zakharko, Y.; Held, M.; Graf, A.; Rödlmeier, T.; Eckstein, R.; Hernandez-Sosa, G.; Hähnlein, B.; Pezoldt, J.; Zaumseil, J. Surface Lattice Resonances for Enhanced and Directional Electroluminescence at High Current Densities. *ACS Photonics* **2016**, *3*, 2225−2230.

(47) Cotrufo, M.; Osorio, C. I.; Koenderink, A. F. Spin-Dependent Emission from Arrays of Planar Chiral Nanoantennas Due to Lattice and Localized Plasmon Resonances. *ACS Nano* **2016**, *10*, 3389−3397.

(48) Schokker, A. H.; van Riggelen, F.; Hadad, Y.; Alù, A.; Koenderink, A. F. Systematic Study of the Hybrid Plasmonic-Photonic Band Structure Underlying Lasing Action of Diffractive Plasmon Particle Lattices. *Phys. Rev. B: Condens. Matter Mater. Phys.* **2017**, *95*, 085409.

(49) Wang, D.; Yang, W.; Wang, Ankunand; Hua, R. D.; Schaller, Yiand; Schatz, G. C.; Odom, T. W. Band-Edge Engineering for Controlled Multi-Modal Nanolasing in Plasmonic Superlattices. *Nat. Nanotechnol.* **2017**, *12*, 889.

(50) Guo, R.; Nečada, M.; Hakala, T. K.; Väkeväinen, A. I.; Törmä, P. Lasing at *K* Points of a Honeycomb Plasmonic Lattice. *Phys. Rev. Lett.* **2019**, *122*, 013901.

(51) Hu, J.; Wang, D.; Bhowmik, D.; Liu, T.; Deng, S.; Knudson, M. P.; Ao, X.; Odom, T. W. Lattice-Resonance Metalenses for Fully Reconfigurable Imaging. *ACS Nano* **2019**, *13*, 4613−4620.

(52) Olson, J.; Manjavacas, A.; Basu, T.; Huang, D.; Schlather, A. E.; Zheng, B.; Halas, N. J.; Nordlander, P.; Link, S. High Chromaticity

Aluminum Plasmonic Pixels for Active Liquid Crystal Displays. *ACS Nano* **2016**, *10*, 1108−1117.

(53) Kristensen, A.; Yang, J. K. W.; Bozhevolnyi, S. I.; Link, S.; Nordlander, P.; Halas, N. J.; Mortensen, N. A. Plasmonic Colour Generation. *Nat. Rev. Mater.* **2017**, *2*, 16088.

(54) Esposito, M.; Todisco, F.; Bakhti, S.; Passaseo, A.; Tarantini, I.; Cuscunà, M.; Destouches, N.; Tasco, V. Symmetry Breaking in Oligomer Surface Plasmon Lattice Resonances. *Nano Lett.* **2019**, *19*, 1922−1930.

(55) Adato, R.; Yanik, A. A.; Amsden, J. J.; Kaplan, D. L.; Omenetto, F. G.; Hong, M. K.; Erramilli, S.; Altug, H. Ultra-Sensitive Vibrational Spectroscopy of Protein Monolayers with Plasmonic Nanoantenna Arrays. *Proc. Natl. Acad. Sci. U. S. A.* **2009**, *106*, 19227−19232.

(56) Thackray, B. D.; Kravets, V. G.; Schedin, F.; Auton, G.; Thomas, P. A.; Grigorenko, A. N. Narrow Collective Plasmon Resonances in Nanostructure Arrays Observed at Normal Light Incidence for Simplified Sensing in Asymmetric Air and Water Environments. *ACS Photonics* **2014**, *1*, 1116−1126.

(57) Danilov, A.; Tselikov, G.; Wu, F.; Kravets, V. G.; Ozerov, I.; Bedu, F.; Grigorenko, A. N.; Kabashin, A. V. Ultra-Narrow Surface Lattice Resonances in Plasmonic Metamaterial Arrays for Biosensing Applications. *Biosens. Bioelectron.* **2018**, *104*, 102−112.

(58) Väkeväinen, A. I.; Moerland, R. J.; Rekola, H. T.; Eskelinen, A.-P.; Martikainen, J.-P.; Kim, D.-H.; Törmä, P. Plasmonic Surface Lattice Resonances at the Strong Coupling Regime. *Nano Lett.* **2014**, *14*, 1721−1727.

(59) Todisco, F.; Esposito, M.; Panaro, S.; De Giorgi, M.; Dominici, L.; Ballarini, D.; Fernández-Domínguez, A. I.; Tasco, V.; Cuscunà, M.; Passaseo, A.; Ciracì, C.; Gigli, G.; Sanvitto, D. Toward Cavity Quantum Electrodynamics with Hybrid Photon Gap-Plasmon States. *ACS Nano* **2016**, *10*, 11360−11368.

(60) Rodriguez, S. R. K.; Feist, J.; Verschuuren, M. A.; Garcia Vidal, F. J.; Gómez Rivas, J. Thermalization and Cooling of Plasmon-Exciton Polaritons: Towards Quantum Condensation. *Phys. Rev. Lett.* **2013**, *111*, 166802.

(61) Ramezani, M.; Halpin, A.; Fernández-Domínguez, A. I.; Feist, J.; Rodriguez, S. R.-K.; Garcia-Vidal, F. J.; Rivas, J. G. Plasmon-Exciton-Polariton Lasing. *Optica* **2017**, *4*, 31−37.

(62) Hakala, T. K.; Moilanen, A. J.; Väkeväinen, A. I.; Guo, R.; Martikainen, J.-P.; Daskalakis, K. S.; Rekola, H. T.; Julku, A.; Törmä, P. Bose−Einstein Condensation in a Plasmonic Lattice. *Nat. Phys.* **2018**, *14*, 739−744.

(63) Humphrey, A. D.; Meinzer, N.; Starkey, T. A.; Barnes, W. L. Surface Lattice Resonances in Plasmonic Arrays of Asymmetric Disc Dimers. *ACS Photonics* **2016**, *3*, 634−639.

(64) Humphrey, A. D.; Barnes, W. L. Plasmonic Surface Lattice Resonances in Arrays of Metallic Nanoparticle Dimers. *J. Opt.* **2016**, *18*, 035005.

(65) Mahi, N.; Lèvêque, G.; Saison, O.; Marae-Djouda, J.; Caputo, R.; Gontier, A.; Maurer, T.; Adam, P.-M.; Bouhafs, B.; Akjouj, A. In Depth Investigation of Lattice Plasmon Modes in Substrate-Supported Gratings of Metal Monomers and Dimers. *J. Phys. Chem. C* **2017**, *121*, 2388−2401.

(66) Zhou, W.; Odom, T. W. Tunable Subradiant Lattice Plasmons by Out-Of-Plane Dipolar Interactions. *Nat. Nanotechnol.* **2011**, *6*, 423.

(67) Zhou, W.; Hua, Y.; Huntington, M. D.; Odom, T. W. Delocalized Lattice Plasmon Resonances Show Dispersive Quality Factors. *J. Phys. Chem. Lett.* **2012**, *3*, 1381−1385.

(68) Huttunen, M. J.; Dolgaleva, K.; Törmä, P.; Boyd, R. W. Ultra-Strong Polarization Dependence of Surface Lattice Resonances with Out-Of-Plane Plasmon Oscillations. *Opt. Express* **2016**, *24*, 28279−28289.

(69) Rodriguez, S. R. K.; Abass, A.; Maes, B.; Janssen, O. T. A.; Vecchi, G.; Gómez Rivas, J. Coupling Bright and Dark Plasmonic Lattice Resonances. *Phys. Rev. X* **2011**, *1*, 021019.

(70) Liu, J.-Q.; He, M.-D.; Wang, D.-Y.; Tang, X.-M.; Zhang, X.-J.; Zhu, Y.-Y. Sharp Plasmonic Resonances Based on Coupling of High Order Localized Resonance and Lattice Surface Mode in Meta-Molecules. *J. Phys. D: Appl. Phys.* **2014**, 47, 045303.

(71) Wang, D.; Yang, A.; Hryn, A. J.; Schatz, G. C.; Odom, T. W. Superlattice Plasmons in Hierarchical Au Nanoparticle Arrays. *ACS Photonics* **2015**, *2*, 1789−1794.

(72) Zilio, P.; Malerba, M.; Toma, A.; Zaccaria, R. P.; Jacassi, A.; Angelis, F. D. Hybridization in Three Dimensions: A Novel Route toward Plasmonic Metamolecules. *Nano Lett.* **2015**, *15*, 5200−5207.

(73) Hakala, T. K.; Rekola, H. T.; Väkeväinen, A. I.; Martikainen, J.-P.; Nečada, M.; Moilanen, A. J.; Törmä, P. Lasing in Dark and Bright Modes of a Finite-Sized Plasmonic Lattice. *Nat. Commun.* **2017**, *8*, 13687.

(74) Li, R.; Bourgeois, M. R.; Cherqui, C.; Guan, J.; Wang, D.; Hu, J.; Schaller, R. D.; Schatz, G. C.; Odom, T. W. Hierarchical Hybridization in Plasmonic Honeycomb Lattices. *Nano Lett.* **2019**, *19*, 6435−6441.

(75) Lin, Y.; Wang, D.; Hu, J.; Liu, J.; Wang, W.; Guan, J.; Schaller, R. D.; Odom, T. W. Engineering Symmetry-Breaking Nanocrescent Arrays for Nanolasing. *Adv. Funct. Mater.* **2019**, *29*, 1904157.

(76) Tan, T. C. W.; Plum, E.; Singh, R. Lattice-Enhanced Fano Resonances from Bound States in the Continuum Metasurfaces. *Adv. Opt. Mater.* **2020**, *8*, 1901572.

(77) Liu, S.-D.; Yue, P.; Zhang, S.; Wang, M.; Dai, H.; Chen, Y.; Nie, Z.-Q.; Cui, Y.; Han, J.-B.; Duan, H. Metasurfaces Composed of Plasmonic Molecules: Hybridization between Parallel and Orthogonal Surface Lattice Resonances. *Adv. Opt. Mater.* **2020**, *8*, 1901109.

(78) Teperik, T. V.; Degiron, A. Design Strategies to Tailor the Narrow Plasmon-Photonic Resonances in Arrays of Metallic Nanoparticles. *Phys. Rev. B: Condens. Matter Mater. Phys.* **2012**, *86*, 245425.

(79) García de Abajo, F. J. Multiple Scattering of Radiation in Clusters of Dielectrics. *Phys. Rev. B: Condens. Matter Mater. Phys.* **1999**, *60*, 6086−6102.

(80) Johnson, P. B.; Christy, R. W. Optical Constants of the Noble Metals. *Phys. Rev. B* **1972**, *6*, 4370−4379.

(81) Baur, S.; Sanders, S.; Manjavacas, A. Hybridization of Lattice Resonances. *ACS Nano* **2018**, *12*, 1618−1629.

(82) Kolkowski, R.; Koenderink, A. F. Lattice Resonances in Optical Metasurfaces with Gain and Loss. *Proceedings of the IEEE* **2019**, 1−24.

(83) Becerril, D.; Vázquez, O.; Piccotti, D.; Sandoval, E. M.; Cesca, T.; Mattei, G.; Noguez, C.; Pirruccio, G. Diffractive Dipolar Coupling in Non-Bravais Plasmonic Lattices. *Nanoscale Adv.* **2020**, *2*, 1261−1268.

(84) Fradkin, I. M.; Dyakov, S. A.; Gippius, N. A. Nanoparticle Lattices with Bases: Fourier Modal Method and Dipole Approximation. *Phys. Rev. B: Condens. Matter Mater. Phys.* **2020**, *102*, 045432.

(85) Thongrattanasiri, S.; Koppens, F. H. L.; García de Abajo, F. J. Complete Optical Absorption in Periodically Patterned Graphene. *Phys. Rev. Lett.* **2012**, *108*, 047401.

(86) Abujetas, D. R.; van Hoof, N.; ter Huurne, S.; Rivas, J. G.; Sánchez-Gil, J. A. Spectral and Temporal Evidence of Robust Photonic Bound States in the Continuum on Terahertz Metasurfaces. *Optica* **2019**, *6*, 996−1001.

(87) Tretyakov, S. Maximizing Absorption and Scattering by Dipole Particles. *Plasmonics* **2014**, *9*, 935−944.

(88) Alabastri, A.; Malerba, M.; Calandrini, E.; Manjavacas, A.; De Angelis, F.; Toma, A.; Proietti Zaccaria, R. Controlling the Heat Dissipation in Temperature-Matched Plasmonic Nanostructures. *Nano Lett.* **2017**, *17*, 5472−5480.

(89) Rodriguez, S. R. K.; Schaafsma, M. C.; Berrier, A.; Gómez-Rivas, J. Collective Resonances in Plasmonic Crystals: Size Matters. *Phys. B* **2012**, *407*, 4081−4085.

(90) Martikainen, J.-P.; Moilanen, A. J.; Törmä, P. Coupled Dipole Approximation across the Γ-point in a Finite-Sized Nanoparticle Array. *Philos. Trans. R. Soc., A* **2017**, *375*, 20160316.

(91) Matsushima, A. Effect of Periodicity in the Light Scattering From Infinite and Finite Arrays of Silver Nanospheres. *Proc. of 2017 IEEE International Conference on Computational Electromagnetics (ICCEM)* **2017**, 236−237.

(92) Zundel, L.; Manjavacas, A. Finite-Size Effects on Periodic Arrays of Nanostructures. *J. Phys.: Photonics* **2019**, *1*, 015004.

(93) Zakomirnyi, V. I.; Ershov, A. E.; Gerasimov, V. S.; Karpov, S. V.; Ågren, H.; Rasskazov, I. L. Collective Lattice Resonances in Arrays of Dielectric Nanoparticles: A Matter of Size. *Opt. Lett.* **2019**, *44*, 5743−5746.

(94) Wang, D.; Bourgeois, M. R.; Guan, J.; Fumani, A. K.; Schatz, G. C.; Odom, T. W. Lasing from Finite Plasmonic Nanoparticle Lattices. *ACS Photonics* **2020**, *7*, 630−636.

(95) Auguié, B.; Bendaña, X. M.; Barnes, W. L.; García de Abajo, F. J. Diffractive Arrays of Gold Nanoparticles near an Interface: Critical Role of the Substrate. *Phys. Rev. B: Condens. Matter Mater. Phys.* **2010**, *82*, 155447.

Supporting Information: Super- and Subradiant Lattice Resonances in Bipartite Nanoparticle Arrays

Alvaro Cuartero-González,[†] Stephen Sanders,[‡] Lauren Zundel,[‡] Antonio I. Fernández-Domínguez,[†] and Alejandro Manjavacas*,[‡]

†*Departamento de Física Teórica de la Materia Condensada and Condensed Matter Physics Center (IFIMAC), Universidad Autónoma de Madrid, E-28049 Madrid, Spain*

‡*Department of Physics and Astronomy, University of New Mexico, Albuquerque, New Mexico 87106, United States*

E-mail: manjavacas@unm.edu

Comparison of the Coupled Dipole Model with Fully Numerical Calculations

In order to benchmark the results from the coupled dipole model (CDM), we compare it against rigorous numerical solutions of Maxwell's equations obtained using a finite element method (FEM) approach implemented in the commercial software COMSOL Multiphysics (see Fig. S1). In all of the cases, the nanoparticle arrays are located in the xy-plane and illuminated with an incident plane wave propagating along the positive z-axis and polarized along the x-direction. Under these conditions, there is a fourfold reflection symmetry that allows us to restrict the simulation domain to one quarter of the array unit cell. We choose the boundaries of the simulation domain parallel to the yz- and xz-planes as perfect electric and perfect magnetic conductors, respectively. Furthermore, to truncate the simulation

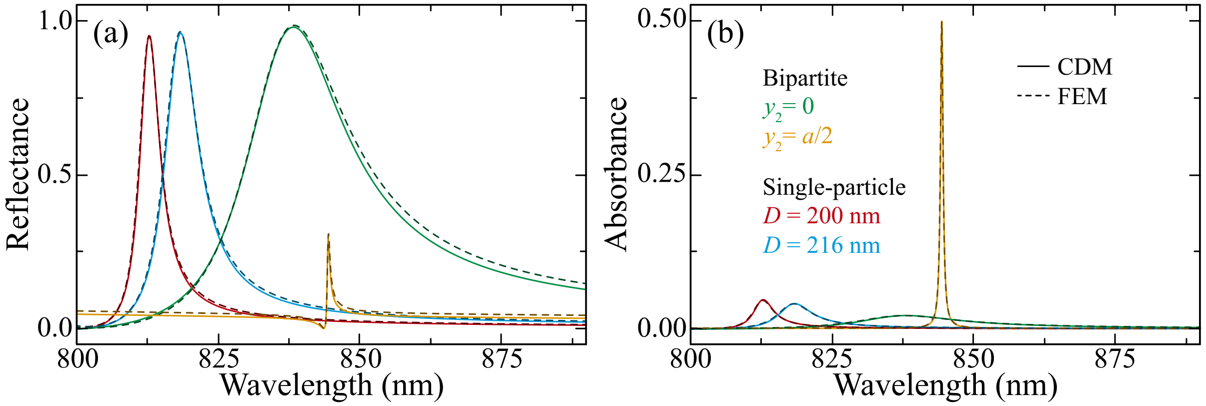

Figure S1: Comparison of the coupled dipole model (CDM, solid curves) with rigorous solutions of Maxwell's equations obtained using a finite element method approach (FEM, dashed curves). We plot the reflectance (a) and absorbance (b) for the same arrays investigated in Figure 1. Specifically, the green and yellow curves display the results for a bipartite array with period $a = 800\,\mathrm{nm}$ and particle diameters $D_1 = 200\,\mathrm{nm}$ and $D_2 = 216\,\mathrm{nm}$. In both cases, $x_2 = a/2$, while y_2 is either 0 (green curve) or $a/2$ (yellow curve). Similarly, the red and blue curves show the results for a single-particle array with the same periodicity a, made of particles with diameter D_1 (red curve) or D_2 (blue curve). In all cases, we assume illumination at normal incidence with polarization along the x-axis. These results demonstrate the accuracy of the CDM.

domain in the z-direction, we use perfectly matched layers (PML). Upon solving Maxwell's equations, we obtain the value of the electric and magnetic fields at all points in the simulation domain. Using these solutions, we calculate the absorbance of the array as the ratio between the total power dissipated in the unit cell and the incident power. Similarly, we obtain the transmittance and reflectance from the power leaving the simulation domain along the positive and negative z-axis, normalized to the incident power. All of the calculations are checked for convergence with respect to the size of the simulation domain as well as the mesh size.

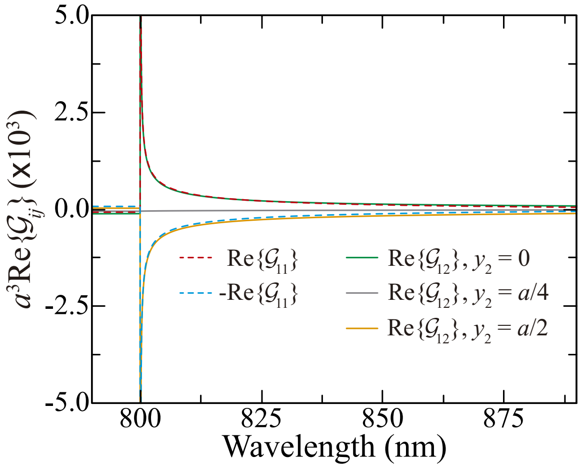

Figure S2: Spectral dependence of the real part of the lattice sums $\mathrm{Re}\{\mathcal{G}_{11}\}$ and $\mathrm{Re}\{\mathcal{G}_{12}\}$. In all cases, we consider arrays with periodicity $a = 800\,\mathrm{nm}$, and assume normal incidence. Dashed curves are used to display $\mathrm{Re}\{\mathcal{G}_{11}\}$ (red curve) and $-\mathrm{Re}\{\mathcal{G}_{11}\}$ (blue curve), whereas solid curves indicate the value of $\mathrm{Re}\{\mathcal{G}_{12}\}$ for $y_2 = 0$ (green curve), $y_2 = a/4$ (gray curve), and $y_2 = a/2$ (yellow curve). These results show that $\mathrm{Re}\{\mathcal{G}_{12}\} \approx \mathrm{Re}\{\mathcal{G}_{11}\}$ for $y_2 = 0$, $\mathrm{Re}\{\mathcal{G}_{12}\} \ll \mathrm{Re}\{\mathcal{G}_{11}\}$ for $y_2 = a/4$, and $\mathrm{Re}\{\mathcal{G}_{12}\} \approx -\mathrm{Re}\{\mathcal{G}_{11}\}$ for $y_2 = a/2$.

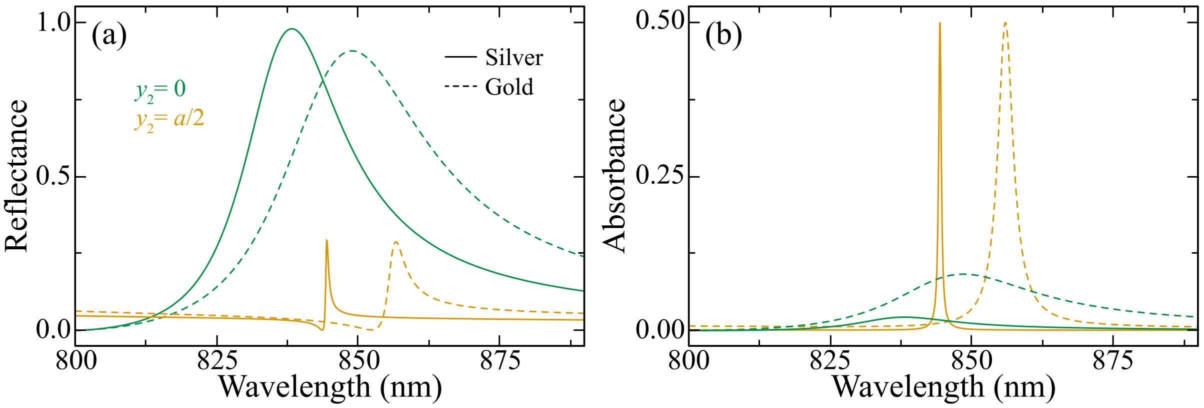

Figure S3: Analysis of the effect of the material properties of the lattice resonances supported by bipartite arrays. We plot the reflectance (a) and absorbance (b) for bipartite arrays with period $a = 800\,\mathrm{nm}$ made of silver (solid curves) or gold (dashed curves) nanoparticles. Green and yellow curves display the results corresponding to the super- (*i.e.*, $y_2 = 0$) and subradiant (*i.e.*, $y_2 = a/2$) arrays, respectively. In all cases, the diameter of particle 1 is $D_1 = 200\,\mathrm{nm}$, while $D_2 = 216\,\mathrm{nm}$ for the silver array and $D_2 = 236\,\mathrm{nm}$ for the gold one. These diameters are chosen such that the subradiant array displays maximum absorbance. We assume illumination at normal incidence with polarization along the x-axis. Both silver and gold arrays display similar values of reflectance and absorbance, although the larger material losses of gold as compared with silver result in broader lineshapes.

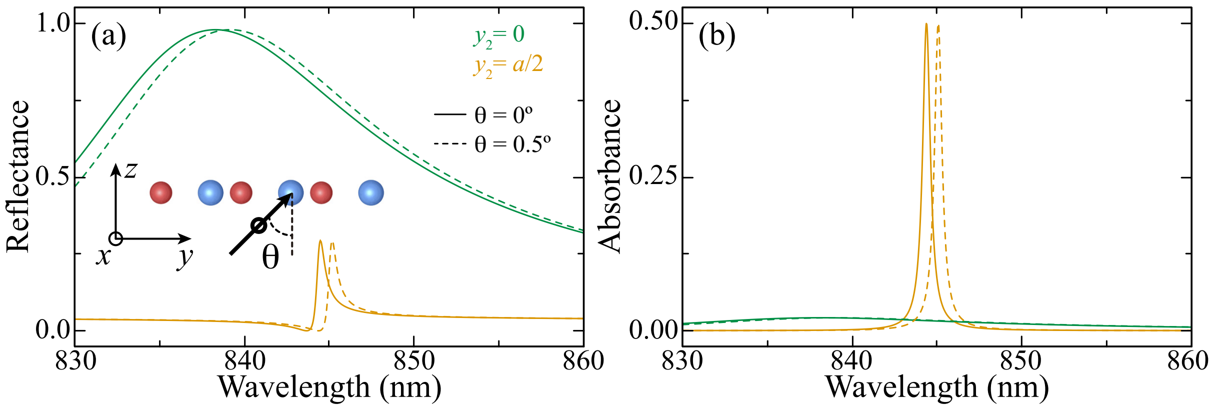

Figure S4: Analysis of the effect of oblique incidence on the lattice resonances supported by bipartite arrays. We plot the reflectance (a) and absorbance (b) for bipartite arrays with period $a = 800\,\mathrm{nm}$ made of nanoparticles with $D_1 = 200\,\mathrm{nm}$ and $D_2 = 216\,\mathrm{nm}$. Green and yellow curves display the results corresponding to the super- (*i.e.*, $y_2 = 0$) and subradiant (*i.e.*, $y_2 = a/2$) arrays, respectively. We analyze the response of these arrays under normal (*i.e.*, $\theta = 0^\circ$, solid lines) and oblique incidence with $\theta = 0.5^\circ$ (dashed curves), as indicated in the inset. In all cases, the polarization of the incident field is along the x-axis. Due to its extremely narrow lineshape, the subradiant lattice resonance is shifted by approximately its linewidth when the angle of incidence is tilted by 0.5°. This limits the numerical aperture of the excitation beam to be $\lesssim 10^{-2}$.